Interchannel coupling induced gapless modes in multichannel zero-line systems

Yulei Han [1,2,*] Sanyi You,[2,*] and Zhenhua Qiao [2,†]

[1]*Department of Physics, Fuzhou University, Fuzhou, Fujian 350108, China*

[2]*ICQD, Hefei National Laboratory for Physical Sciences at the Microscale, CAS Key Laboratory of Strongly Coupled Quantum Matter Physics, and Department of Physics, University of Science and Technology of China, Hefei, Anhui 230026, China*

(Received 3 November 2021; revised 24 March 2022; accepted 25 March 2022; published 4 April 2022)

In bilayer graphene, the application of a perpendicular electric field breaks the inversion symmetry to open a bulk band gap to harbor the quantum valley Hall effect. When the field varies spatially, a topologically confined mode (also named the zero-line mode) arises along the zero-field line. In this work, we theoretically investigate the electronic transport properties of the multichannel zero-line systems. The finite-size effect in topological systems (e.g., quantum Hall effect, topological insulators) often induces a topologically trivial gap to realize a normal insulator. To our surprise, we find that the coupling between neighboring zero lines can give rise to striking electronic properties depending on the number of channels m, i.e., a trivial band gap for even m, whereas a nontrivial gapless mode for odd m. We further show that these findings apply to various ribbon orientations. A general effective model is constructed to provide a clear physical picture of the emergence of gapless modes. In the end, a gate-tunable device is proposed to function as a switch with controllable current partitions. We believe that our findings are experimentally accessible, and have potential practical applications in designing multifunctional valley-based electronics.

DOI: 10.1103/PhysRevB.105.155301

I. INTRODUCTION

A monolayer honeycomb lattice with linear Dirac dispersion is an ideal platform to explore various topological phases [1], including the quantum anomalous Hall effect [2], quantum spin Hall effect [3], and quantum valley Hall effect [4]. When a spatially varying electric field is applied to bilayer graphene, the broken inversion symmetry opens a bulk gap, and a one-dimensional (1D) conducting state, also known as the zero-line mode (ZLM), appears at the interface between regions with different valley topologies [5–29]. Theoretical studies have found that the ZLM is quite robust against backscattering with a large mean free path ($\sim$100 μm) [9], and the robustness can be further enhanced by applying an external magnetic field [10]. A single-channel ZLM has been experimentally realized in gated bilayer graphene with line defects [17,18], or by precise gate alignment [19–21], indicating promising potential applications in low-energy-consumption electronics. When two ZLMs form an intersection, it can function as a topological current splitter, in which the splitting of ZLMs follows counterintuitive partition laws [22], and can be effectively tuned by gate voltage or magnetic field [23]. The theoretical findings have been realized experimentally in gate-controlled bilayer graphene systems [24]. The crossing of ZLMs can also be utilized to design Aharonov-Bohm interferometers with valley-polarized electronic states [27] or unique oscillation behavior [28], and to realize topological corner states formed by two different types of ZLMs [29].

Multichannel ZLMs, as demonstrated in Fig. 1, are made up of multiple parallel 1D conducting states. This device architecture can be realized in a 1D graphene/hBN moiré pattern or graphene/hBN heteronanotubes [30–32], and also in bilayer graphene systems with line defects [33,34] or periodic gate alignment [35,36]. The spatial separation of multichannel ZLMs enables it to realize more intricate functions than single-channel ZLMs, such as the topological solenoid [31]. Due to exponential spatial decay of wave functions, multichannel ZLMs can be viewed as the sum over single-channel ZLMs if the distance between neighboring 1D conducting channels d is large enough. However, if d is short, the coupling between adjacent 1D conducting channels can lead to some intriguing physics, e.g., the formation of a band gap in the integer quantum Hall regime [37] or topological insulators [38], and the formation of the second-order topological superconducting phase in the presence of in-plane magnetic field and weakly coupled superconductivity [35].

Besides the gap state induced by interchannel coupling, in this work, we demonstrate that a robust gapless mode can be realized in multichannel ZLMs. We systematically investigate the influence of the number of channels m, the orientation of edges, and disorder effects on the electronic properties of multichannel ZLMs. We find that the interchannel coupling of ZLMs leads to a global band gap when m is even, whereas the system exists in a gapless mode when m is odd, and the parity of m has a significant influence on the wave function distribution. By varying the orientation of nanoribbon edges, we find that the appearance of a gapless mode for odd m is independent of the type of edges except for the armchair

*These authors contributed equally to this work.
†Corresponding author: qiao@ustc.edu.cn

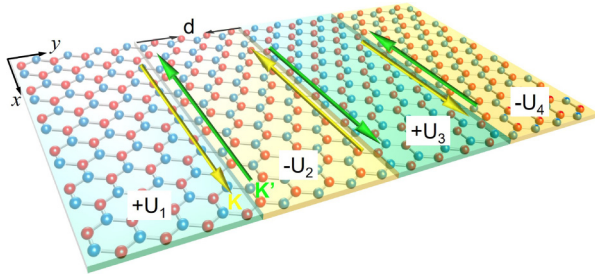

FIG. 1. Schematic plot of a three-channel ($m = 3$) device in monolayer graphene. The device is periodic (open) along x (y) direction. The $\lambda_k U_k$ ($k = 1, 2, 3, 4$) is labeled in each subregion along y direction, where λ_k (U_k) denotes the sign (strength) of staggered sublattice potential. d measures the distance of adjacent zero-line modes. The yellow and green arrows represent the movement direction of electrons in valleys K and K', respectively.

edge, where a finite band gap opens up due to strong intervalley scattering. And the gapless mode for odd m is quite robust against strong short-range and long-range disorders. Based on the tight-binding results, we construct an effective model to clarify the role of interchannel coupling on electronic properties. We then propose a gate-tunable device that can be used as a switch with controllable current partitions. Based on the recent experimental advances on fabricating multichannel electronic devices either by manipulating line defects [34] or by artificial periodic gates in bilayer graphene systems [36], we believe that these findings can be realized in such systems and directly extended to classical wave graphene systems [39–43].

II. METHODS AND SYSTEMS

Hereafter, we use "m" to denote the number of channels. Figure 1 displays the schematic plot of a three-channel device ($m = 3$) in a monolayer honeycomb lattice with staggered sublattice potential denoted by blue or red color. The multichannel 1D conducting states propagate along the x direction, with a separation distance of d in the y direction. In each subregion, the presence of a staggered sublattice potential breaks the inversion symmetry and opens a bulk band gap, which is equivalent to the effect of vertical electric fields applied in Bernal-stacked bilayer graphene [4,9,22,23]. The corresponding tight-binding Hamiltonian of the multichannel system can be written as [22]

$$H = -t \sum_{\langle i,j \rangle} c_i^\dagger c_j + \lambda_k U_k \left(\sum_{i \in A} c_i^\dagger c_i - \sum_{i \in B} c_i^\dagger c_i \right), \qquad (1)$$

where $c_i^\dagger$ (c_i) is the creation (annihilation) operator on site i, t is the hopping energy between the nearest-neighbor sites, U_k measures the strength of staggered sublattice potential in the kth subregion, and $\lambda_k = (-1)^{k-1}$ denotes the sign of the valley Hall effect in the kth subregion ($k = 1, 2, \ldots, m + 1$). The $\sum_{i \in A/B}$ in the second term represents the sum over the A or B sublattice of monolayer graphene. The ZLMs are located at the lines where λ_k changes sign as displayed in Fig. 1. For simplicity, we set $U_k = U = 0.05t$ unless otherwise specified, and the corresponding band gap of the system is $\varepsilon = 2U$.

III. THE BAND STRUCTURES OF THE MULTICHANNEL ZLMs FOR DIFFERENT m

We first analyze the 1D band structures of the multichannel devices for different m with zigzag edges. In the presence of time-reversal symmetry, a pair of chiral states originating from valleys K and K' exist in each channel. Therefore, we focus on the low-energy regions around valley K, where only ZLMs are visible (see Appendix A for the full band structures of the multichannel ZLMs).

Figure 2 displays the low-energy band structures and the corresponding wave functions of the multichannel devices for different m around valley K. We can find distinct features depending on the parity of m, i.e., a finite band gap for even m, or a gapless mode for odd m. These intriguing features arise from the coupling between adjacent channels. The sign of valley Hall topologies λ_k in a multichannel device can be denoted as "$+ - + - \ldots$", indicating that two adjacent channels have opposite chirality; i.e., the electronic group velocity is positive for one channel and negative for the other channel at the same valley (see Fig. 1). This characteristic is explicitly displayed in Figs. 2(a_1) and 2(a_2) for the two-channel device ($m = 2$). One can find that the states labeled as "A" and "B" have opposite velocities, and their wave functions are well separated along the adjacent channels with a small overlap. For the four-channel system, as displayed in Figs. 2(c_1) and 2(c_2), the modes "A" and "B" have the same chirality and are primarily distributed in the second and fourth channels. Similarly, the modes "C" and "D" are mainly distributed in the first and third channels. We can also observe that a small part of the "B" state is distributed in the first and third channels, indicating that the closer to the valley K, the stronger the interchannel coupling. The systems with even number of channels demonstrate finite interchannel coupling induced gaps, which can be labeled as Δ_i (see Fig. 5).

When $m = 3$, as displayed in Figs. 2(b_1) and 2(b_2), we can define three types of ZLMs (labeled as "A", "B", and "C"). The "A" state primarily located at the second channel has a negative group velocity, whereas the "B" and "C" states located at the first and third channels have positive group velocities. It is noteworthy that around the charge neutrality point of $E/t = 0$, the wave function of the gapless mode "C" is averagely distributed in the two channels with the same chirality, indicating a coherent electronic state in these channels. This characteristic can also be observed in the case of $m = 5$ [see Figs. 2(d_1) and 2(d_2)], where the wave function of the gapless mode labeled as "E" is averagely distributed in the three channels with the same chirality, i.e., the first, third, and fifth channels. As shown in Fig. 2(d_2), we can also find that the modes denoted as "A" and "B" are mainly distributed in the second and fourth channels with the same chirality, whereas the modes "C" and "D" are mainly distributed in the remaining channels. It is worth noting that the wave function distribution of the gapless mode is k-independent, whereas the wave function distributions of the other modes are k-dependent.

The interchannel coupling, determined by the overlap of wave functions between adjacent channels, is crucial to the fascinating states in low-energy regions, i.e., a gap for even m and a gapless mode for odd m. The coupling strength is

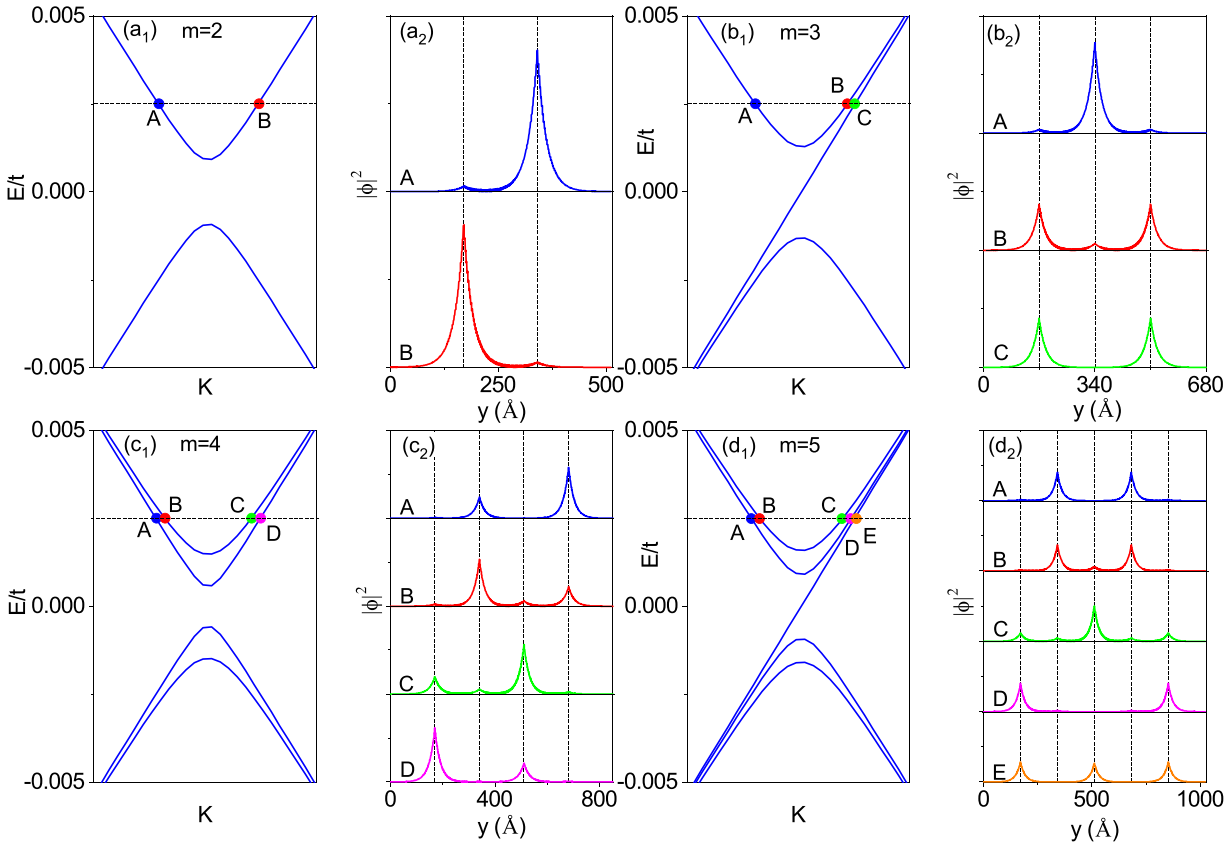

FIG. 2. (a_1)–(d_1): The one-dimensional zero-line modes in low-energy region around valley K, and (a_2)–(d_2): the corresponding wave functions along y direction of the multichannel device for different m. (a_1), (a_2): For $m = 2$; (b_1), (b_2): for $m = 3$; (c_1), (c_2): for $m = 4$; (d_1), (d_2): for $m = 5$. The horizontal black dashed lines in (a_1)–(d_1) represent $E/t = 0.0025$. The vertical black dashed lines in (a_2)–(d_2) represent the position of channels. The gapless mode is labeled as "C" in (b_1) and (b_2), and is labeled as "E" in (d_1) and (d_2). The distance of the adjacent channels is $d = 16.90$ nm.

proportional to e^{-Ud} [23,47]. We then quantitatively study the dependence of coupling strength on system parameters, i.e., d and m. As d increases, the interchannel coupling induced gaps Δ_i/t exponentially decay, indicating that the coupling of wave functions is negligible when $d > 30$ nm with a vanishingly small Δ_i/t in the magnitude of 10^{-5} (see Appendix B).

IV. THE INFLUENCE OF EDGE ORIENTATIONS AND DISORDERS

The edge orientations and disorders are two crucial aspects for the experimental realization of multichannel systems. The presence of ZLMs in valleys K and K' is protected by the large momentum separation. When the edge orientation gradually deviates from the zigzag type, we find that the neighboring valleys K and K' gradually move toward each other in an attractive manner, accompanied by a cross of ZLMs. When the edge evolves into armchair type, the complete mixing of the two valleys induces a strong intervalley scattering, leading to a small avoided crossing gap around the charge neutrality point (see Appendix C). Therefore, the arbitrariness of the edge orientations does not affect the electronic properties of multichannel ZLMs except for the armchair edge.

To study the influence of disorders on electronic transport properties, we consider short-range Anderson disorder and long-range disorder. The Anderson disorder is included as $H_d = \sum_i w_i c_i^\dagger c_i$, where w_i is uniformly distributed in the range of $[-W/2, W/2]$ with W measuring the disorder strength. The long-range disorder is added to the Hamiltonian (1) by including the on-site potential $V_i = \sum_{j=1}^{N_{\rm imp}} w_j \exp(-|\mathbf{r}_j - \mathbf{r}_i|^2/2\xi^2)$ [9], where $\mathbf{r}_i$ denotes a lattice site, $N_{\rm imp}$ represents the number of random Gaussian disorder with a width of $\xi = 5a$ ($a = 1.42$ Å), and w_j is uniformly distributed in the range of $[-W/2, W/2]$ with W measuring the disorder strength. This type of disorder can mimic the effect of charged impurities from substrate inhomogeneities [44]. In our calculations, a dense concentration (1%) of long-range disorder is adopted. The two-terminal conductance can be evaluated by the Landauer-Büttiker formula [45], $G = (e^2/h){\rm Tr}(\Gamma_L G^r \Gamma_R G^a)$, where $G^{r,a}$ are the retarded and advanced Green's functions of the central disordered region, and $\Gamma_{L/R} = i(\sum_{L/R}^r - \sum_{L/R}^a)$ are the linewidth functions coupling left/right terminals to the central region. $\sum^{r/a}$ is the retarded/advanced self-energy of the semi-infinite lead that can be obtained by using the variant transfer matrix method [46].

Figure 3 demonstrates the averaged conductance as a function of device length along the x direction for different disorder strengths. To explore the robustness of the gapless mode, the Fermi level is set to the charge neutrality point ($E/t = 0.0$). In the presence of Anderson disorder, the

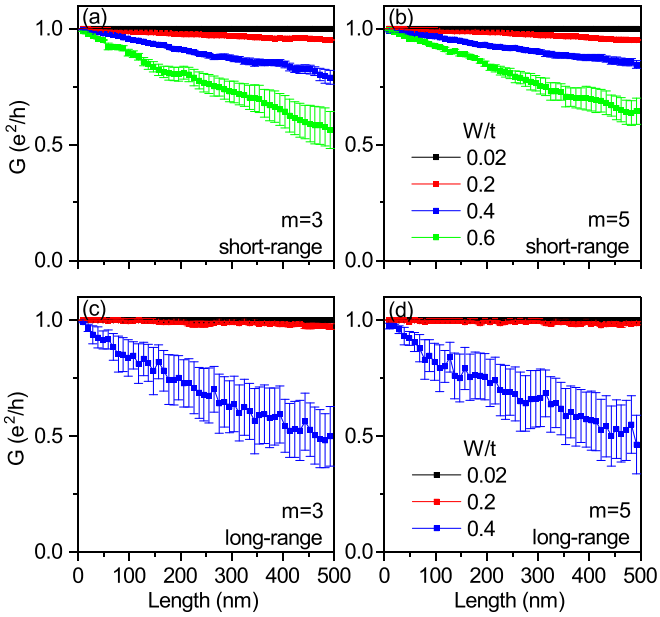

FIG. 3. Averaged conductance as a function of device length for different disorder strengths. (a) and (b): For short-range disorder with strength of $W/t = 0.02, 0.2, 0.4, 0.6$. (c) and (d): For long-range disorder with strength of $W/t = 0.02, 0.2, 0.4$. The Fermi level is set to the charge neutrality point. The distance of the adjacent zero-line modes with zigzag edge is $d = 16.9$ nm. Each point is collected by 80 samples for short-range disorder and by 160 samples for long-range disorder.

averaged conductance for the three-channel device respectively reaches about $0.95\,e^2/h$, $0.79\,e^2/h$, and $0.56\,e^2/h$, whereas the averaged conductance for the five-channel device respectively approaches about $0.95\,e^2/h$, $0.85\,e^2/h$, and $0.64\,e^2/h$ when $W/t = 0.2$, 0.4, and 0.6 at the device length of 500 nm [see Figs. 3(a) and 3(b)]. It is also worth noting that the disorder strength of $W/t = 0.6$ is much larger than the bulk band gap of $\varepsilon/t = 0.1$, meaning that the gapless mode is much more robust against Anderson disorder. In the presence of long-range disorder as shown in Figs. 3(c) and 3(d), the averaged conductance for the three-channel device respectively reaches about $0.97\,e^2/h$ and $0.50\,e^2/h$ when $W/t = 0.2$ and 0.4 at the device length of 500 nm, while the averaged conductance for the five-channel device respectively approaches about $0.99\,e^2/h$ and $0.46\,e^2/h$. Because the disorder strength of $W/t = 0.2$ is still double that of the bulk band gap, the gapless mode is robust against long-range disorder. Therefore, the robustness of the multichannel ZLMs against edge orientations and disorders indicates that experimental realization of the multichannel devices is highly feasible.

V. EFFECTIVE MODEL OF THE MULTICHANNEL ZLMs

To better understand the numerical results based on the tight-binding model, we construct an effective model of the multichannel ZLMs. Based on the basis of each ZLM, the general Hamiltonian can be written as a tridiagonal matrix [47]:

$$H(k) = \begin{pmatrix} \tau\hbar v_F k & \Delta_{12} & 0 & 0 & \\ \Delta_{21} & -\tau\hbar v_F k & \Delta_{23} & 0 & .. \\ 0 & \Delta_{32} & \tau\hbar v_F k & \Delta_{34} & .. \\ 0 & 0 & \Delta_{43} & -\tau\hbar v_F k & \\ & \vdots & \vdots & & \end{pmatrix}_{m\times m}, \quad (2)$$

where the diagonal elements $\pm\tau\hbar v_F k$ describe the kinetic energy of each ZLM with valley index $\tau = \pm 1$. The subdiagonal term Δ_{ij} denotes the coupling between adjacent ith and jth ZLMs, and satisfies the following conditions: $\Delta_{ij} = \Delta_{ji}$, $\Delta_{ij} \propto e^{-U_{ij}d_{ij}}$, where U_{ij} and d_{ij} denote the strength of staggered sublattice potential and interchannel distance between ith and jth ZLMs, respectively. Analytically, it is difficult to directly diagonalize the matrix when $m > 3$. However, without solving the eigenequation, a rigorous proof of the existence of the 1D gapless mode in an odd number of zero-line systems can be derived. The general eigenequation $|H - EI| = 0$ can be written as

$$\begin{vmatrix} \tau\hbar v_F k - E & \Delta_{12} & 0 & 0 & \\ \Delta_{21} & -\tau\hbar v_F k - E & \Delta_{23} & 0 & .. \\ 0 & \Delta_{32} & \tau\hbar v_F k - E & \Delta_{34} & .. \\ 0 & 0 & \Delta_{43} & -\tau\hbar v_F k - E & \\ & \vdots & \vdots & & \end{vmatrix}_{m\times m} = 0. \quad (3)$$

After expanding the first row, we expand the algebraic cofactor of Δ_{12} according to the first column, then the determinant is reduced to $(m-2)$ dimensions, and we get $(\tau\hbar v_F k - E)A_1 + \Delta_{12}(-1)^{1+2}\Delta_{21}B_1 = 0$, where A_1 is the algebraic cofactor of $(\tau\hbar v_F k - E)$ and is not important in our analysis. Iteratively, $B_1 = (-1)^{1+1}[(\tau\hbar v_F k - E)A_2 + \Delta_{34}(-1)^{1+2}\Delta_{43}B_2]$. Repeating the process above, when m is even, we have

$$B_{m/2-1} = (-1)^{1+1}\begin{vmatrix} \tau\hbar v_F k - E & \Delta_{(m-1)(m)} \\ \Delta_{(m)(m-1)} & -\tau\hbar v_F k - E \end{vmatrix} = C_e, \quad (4)$$

where $C_e = (\tau\hbar v_F k - E)(-\tau\hbar v_F k - E) - \Delta^2_{(m-1)(m)}$. When m is odd, we get

$$B_{(m-1)/2-1} = (-1)^{1+1}\begin{vmatrix} \tau\hbar v_F k - E & \Delta_{(m-2)(m-1)} & 0 \\ \Delta_{(m-1)(m-2)} & -\tau\hbar v_F k - E & \Delta_{(m-1)(m)} \\ 0 & \Delta_{(m)(m-1)} & \tau\hbar v_F k - E \end{vmatrix} = (\tau\hbar v_F k - E)C_o, \quad (5)$$

where $C_o = [(\tau\hbar v_F k - E)(-\tau\hbar v_F k - E) - \Delta^2_{(m-1)(m)} - \Delta^2_{(m-2)(m-1)}]$. It is easy to find that when m is odd, the characteristic polynomial of $H(k)$ has a common factor $(\tau\hbar v_F k - E)$ i.e., $|H - EI| = (\tau\hbar v_F k - E)[A_1 + D] = 0$;

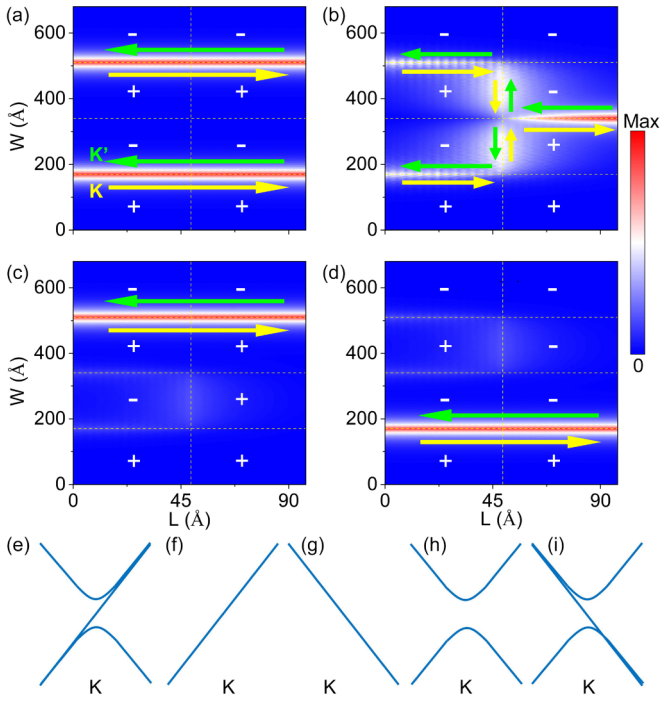

FIG. 4. (a)–(d): Local density of states of the lateral junctions with different valley Hall topologies for $m = 3$ and $E = 0$. The signs of λ_k are shown in each subregion. (e)–(i): Schematic plot of low-energy band structures of the three-channel ZLMs with different valley Hall topologies around valley K. The corresponding configurations are listed in Table I.

then the gapless mode $E = \tau\hbar v_F k$ is obtained. Obviously, when m is even, the absence of such common factor indicates a qualitative difference induced by the parity of m. To clearly show the influence of parity of m, we provide two analytical examples for $m = 2$ and $m = 3$ in Appendix D.

VI. GATE-TUNABLE CURRENT PARTITION AND SWITCH

Based on the unique electronic properties of the multichannel ZLMs, we propose a gate-tunable lateral junction that can function as a switch with controllable current partitions. For the sake of clarity, we fix the number of channels to be $m = 3$, since the results for larger m can be deduced from the simplest case. The signs of λ_k on the left side of the lateral junction are fixed to the configuration of "$+-+-$" (from bottom to top), whereas those on the right side can be arbitrarily tuned, yielding 2^4 different configurations. Only four of the sixteen configurations allow the electrons to transmit with a quantized conductance of e^2/h, as displayed in Figs. 4(a)–4(d), whereas the remaining twelve configurations are insulating. One can find that the current partition can be tuned by changing the sign of λ_k; e.g., when the right side of the junction has the same configuration as the left side [see Fig. 4(a)], the electron flows through both the upper and lower channels with equal amplitude; when reversing the signs of λ_k on the right side to "$++--$" [see Fig. 4(b)], the electrons injecting from the two side channels transmit to the central channel; when the sign of λ_k is changed to "$++-$ ($+--$)", as displayed in Fig. 4(c) [Fig. 4(d)], the electron flows through the upper (lower) channel due to the coherence of the two channels with the same chirality.

TABLE I. The configurations of the three-channel devices for each type of band category as shown in Figs. 4(e)–4(i). The signs of λ_k are used to denote the configurations.

Category	Configurations
(e)	$+-+-$
(f)	$++-+$, $++--$, $+---$
(g)	$-++-$, $--++$, $---+$
(h)	$++-+$, $+-++$, $+--+$, $-+-+$, $-+--$, $--+-$, $+++-$,[a] $----$[a]
(i)	$-+-+$

[a]These configurations are fully gapped without the presence of ZLM.

The intriguing transport properties can be clearly explained by the 1D band structures. For the sixteen configurations, the 1D band structures can be classified into five categories, as shown in Figs. 4(e)–4(i). And the corresponding configurations for each category are listed in Table I. When the sign of λ_k alternately changes to form the "$+-+-$" configuration, the band structure has a gapless mode as discussed before [see Fig. 4(e)], where the electrons are distributed averagely in the two channels with positive chirality as shown in Fig. 4(a). When λ_k is properly tuned to form a single-channel ZLM with positive chirality, as displayed on the right side of Figs. 4(b)–4(d), the band structure can be described as Fig. 4(f), and thus electron can fully transmit through the system since the chirality is the same for both sides of the junction. Besides the above two conducting cases with four configurations, the two-terminal conductances of junctions with other valley Hall topologies vanish because of the absence of allowed channels for the electron to transmit. The remaining twelve configurations as listed in Table I form three types of band structures, as displayed in Figs. 4(g)–4(i), i.e., single-channel ZLM with negative chirality [Fig. 4(g)], two-channel ZLMs with a band gap [Fig. 4(h)], and three-channel ZLMs with negative chirality [Fig. 4(i)]. Therefore, by tuning the signs of λ_k in each subregion, we can realize the valley current switch with controllable current partitions. Because the topological origin of ZLMs in monolayer graphene is the same as that in bilayer graphene, introducing staggered sublattice potential in monolayer graphene is equivalent to applying gate voltage in bilayer graphene. Therefore, the same valley current switch can be feasibly realized in bilayer graphene by applying external gates.

VII. SUMMARY

We theoretically explore the electronic properties of multichannel ZLMs. Due to the finite-size effect, the interchannel coupling can induce a gapless mode for odd m, whereas induce a global band gap for even m, and the parity of m has a significant influence on the wave function distributions. We find that the gapless mode for odd m can be preserved when varying the edge orientations except for the armchair edge, and it is quite robust against both short-range and long-range disorders, indicating that the multichannel devices are feasible to be experimentally realized. By constructing an effective

model, we clearly demonstrate the crucial role of interchannel coupling. Finally, based on the intriguing gapless modes, we propose a promising device that can be utilized to realize gate-tunable electric switch with controllable current partitions. Considering the recent advances in experimental methodologies, we believe that these findings can be realized not only in electronic systems but also in other wavelike systems.

ACKNOWLEDGMENTS

This work was financially supported by the National Natural Science Foundation of China (Grants No. 11974327 and No. 12004369), the Fundamental Research Funds for the Central Universities (Grants No. WK3510000010 and No. WK2030020032), the Education and Research Fund for Young Teachers of Fujian Province (Grant No. JAT210014), the Anhui Initiative in Quantum Information Technologies, and the Startup Funding of Fuzhou University (Grant No. GXRC21066). We are grateful to AMHPC and the Supercomputing Center of USTC for providing the high-performance computing resources.

APPENDIX A: FULL BAND STRUCTURES OF THE MULTICHANNEL ZLMs

Figure 5 displays the full band structures of the multichannel devices with different m. If the gapless mode is ignored, the interchannel coupling induced gaps between conduction and valence bands can be denoted as Δ_i ($i = 1, 2, \ldots$) based on the distance from the charge neutrality point (see inset of Fig. 5). The existence of finite gaps Δ_i indicates that the ZLMs can be selectively activated by tuning the Fermi energy, thus influencing electronic transport properties.

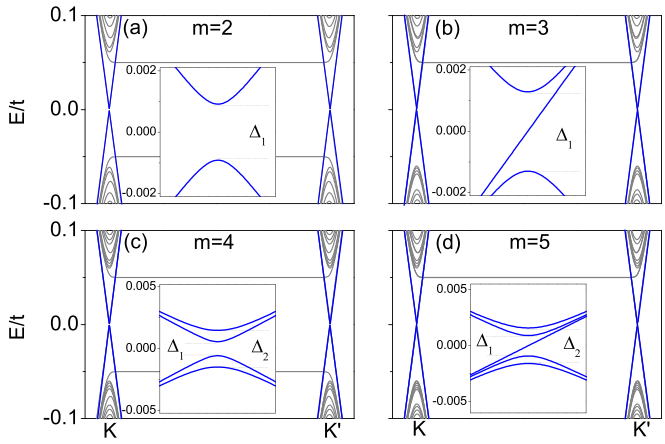

FIG. 5. Full band structures of the multichannel devices with different m. (a) $m = 2$, (b) $m = 3$, (c) $m = 4$, and (d) $m = 5$. The inset displays the zoom-in low-energy bands around K point. Zero-line modes are demonstrated in blue lines. According to the distance from $E/t = 0.0$, the interchannel coupling induced gaps are labeled as Δ_i ($i = 1, 2, \ldots$). The distance of the adjacent zero-line modes is $d = 16.90$ nm and the zigzag termination is adopted.

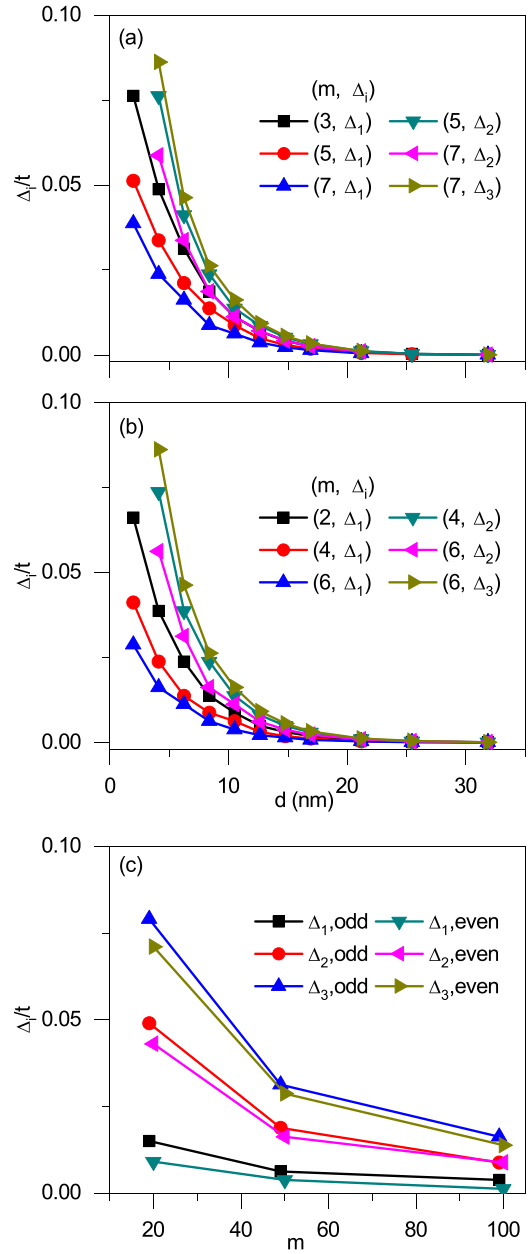

FIG. 6. (a), (b): The interchannel coupling induced gaps Δ_i/t as a function of the distance d for (a) even m and (b) odd m, respectively. (c) The Δ_i/t as a function of m for $d = 1.99$ nm.

APPENDIX B: THE INFLUENCE OF SYSTEM SIZE ON THE INTERCHANNEL COUPLING

Figures 6(a) and 6(b) display the interchannel coupling induced gaps Δ_i/t as a function of the distance d for even and odd m, respectively. As d increases, Δ_i/t exponentially decays, indicating that the coupling of wave functions is negligible when $d > 30$ nm with a vanishingly small Δ/t in the magnitude of 10^{-5}. At a fixed small d, we can find that Δ_i decreases with the increase of m. To clearly show this trend, we calculate the dependence of Δ_i/t on m at a small d, as displayed in Fig. 6(c). One can find that Δ_i gradually decays with the increase of m. When $m = 100$, Δ_1/t is still larger than 10^{-3}, and the energy difference among Δ_i is visible,

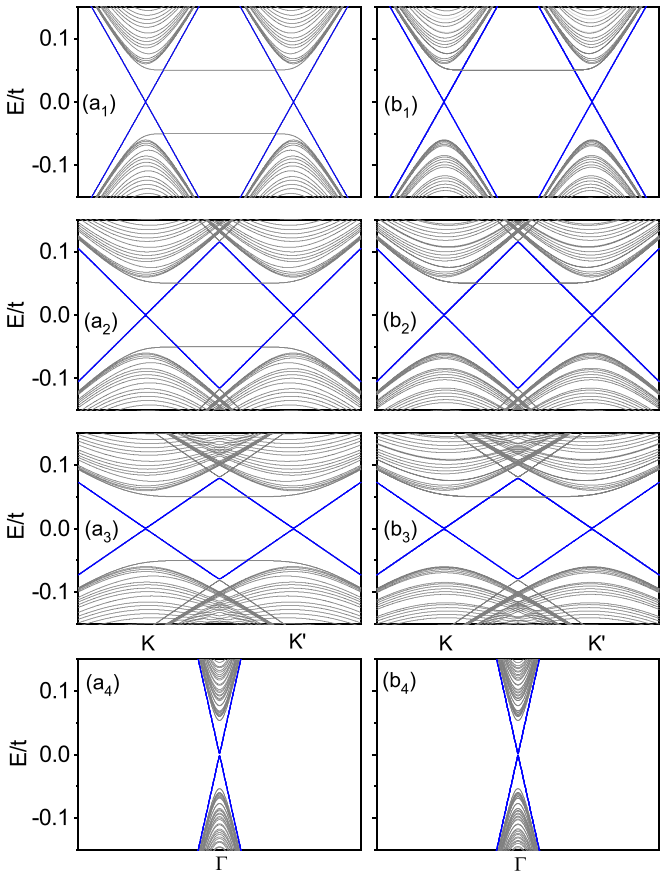

FIG. 7. Band structures of the multichannel devices for (a_1)–(a_4) $m = 4$ and (b_1)–(b_4) $m = 5$ with different edge orientations. Zero-line modes are highlighted in blue. From top to bottom rows, the edge orientations are $(p, q) = (3, 2)$, (5,4), (7,6), and (1,1), respectively, showing a variation from zigzag to armchair edges. The distance of the adjacent zero-line modes is $d = 16.90$ nm.

indicating that the above discussed selective channels of ZLMs can still be tuned by Fermi energy.

APPENDIX C: THE INFLUENCE OF EDGE ORIENTATIONS

Based on the unit vectors of graphene, i.e., $\mathbf{a_1} = (1, 0)a_0$, $\mathbf{a_2} = (1/2, \sqrt{3}/2)a_0$, where $a_0 = 2.46$ Å is the lattice constant, one can tailor arbitrary edges of the nanoribbon with the vector of $\mathbf{r} = p\mathbf{a_1} + q\mathbf{a_2}$; e.g., $(p, q) = (1, 0)$ corresponds to a zigzag edge whereas $(p, q) = (1, 1)$ represents an armchair edge.

Figure 7 displays the band structures of the multichannel device for four types of graphene nanoribbons varying from zigzag to armchair edges, where the edge orientations are $(p, q) = (3, 2)$, (5,4), (7,6), and (1,1), respectively. One can find that the bulk band gaps remain unchanged during the deformation of edges with a value of $2U = 0.1t$. The multichannel ZLMs highlighted in blue appear for the four types of nanoribbons inside the bulk band gaps. When the edge termination deviates from the zigzag type, as illustrated in the first three rows of Fig. 7, the neighboring valleys K and K' gradually move toward each other in an attractive manner, accompanied by a cross of ZLMs. When the edge evolves into armchair type, as displayed in Figs. 7(a_4) and 7(b_4), the valleys K and K' exactly overlap and a finite gap opens up due to strong intervalley scattering.

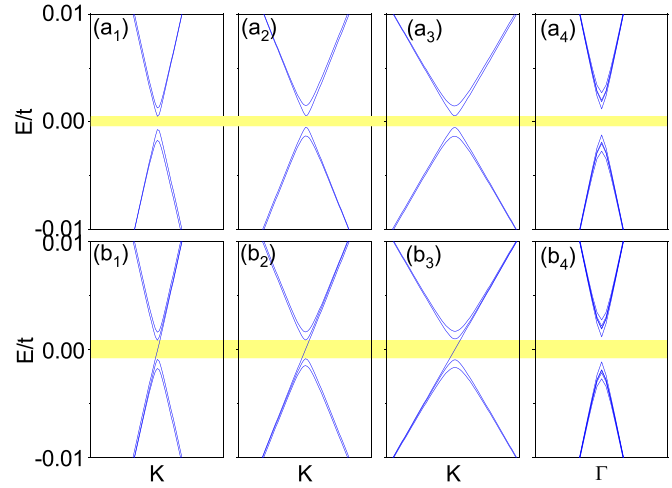

FIG. 8. Zoom-in band structures of Fig. 7 near the charge neutrality point for (a_1)–(a_4) $m = 4$ and (b_1)–(b_4) $m = 5$. The edge orientations are $(p, q) = (3, 2)$, (5,4), (7,6), and (1,1), respectively. The light yellow region represents the interchannel coupling induced gap Δ_1.

Figure 8 shows the zoom-in band of Fig. 7 around the charge neutrality point. For even m, as shown in Figs. 8(a_1)–8(a_3), the interchannel coupling induced gaps always exist, and the gaps Δ_1 remain unchanged during the variation of edge orientations, whereas the gap increases for armchair edge as shown in Fig. 8(a_4) due to the coexistence of interchannel coupling and strong intervalley scattering. For odd m, as displayed in Figs. 8(b_1)–8(b_3), the gapless modes always survive and the gaps Δ_1 remain fixed when the edges are not armchair type. Therefore, the arbitrariness of edge orientations does not affect the electronic properties of multichannel ZLMs except for the armchair edge, indicating the high feasibility of experimental realization of the multichannel devices.

APPENDIX D: TWO ANALYTICAL EXAMPLES OF THE EFFECTIVE MODEL

We consider the case of $m = 2$ and $m = 3$. For $m = 2$, the effective Hamiltonian can be written as

$$H(k)_{m=2} = \begin{pmatrix} \tau\hbar v_F k & \Delta_{12} \\ \Delta_{21} & -\tau\hbar v_F k \end{pmatrix}. \tag{D1}$$

It is easy to find the eigenvalues of $E = \pm\sqrt{(\hbar v_F k)^2 + \Delta_{12}^2}$ and eigenstates of $\Psi_\pm = [(E \pm \tau\hbar v_F k)/\Delta_{12}, 1]' e^{ikx}$. We can find the interchannel coupling induced gap of $2\Delta_{12}$.

For $m = 3$, the effective model can be described as

$$H(k)_{m=3} = \begin{pmatrix} \tau\hbar v_F k & \Delta_{12} & 0 \\ \Delta_{21} & -\tau\hbar v_F k & \Delta_{23} \\ 0 & \Delta_{32} & \tau\hbar v_F k \end{pmatrix}. \tag{D2}$$

The eigenvalues are $E_1 = \tau\hbar v_F k$, $E_{2\pm} = \pm\sqrt{(\hbar v_F k)^2 + \Delta_{12}^2 + \Delta_{23}^2}$, and the corresponding eigenstates are $\Psi_1 = [-\Delta_{23}/\Delta_{12}, 0, 1]' e^{ikx}$, $\Psi_{2\pm} = [\Delta_{12}/\Delta_{23}, (\pm E -$

$\tau\hbar v_F k)/\Delta_{23}, 1]' e^{ikx}$. A gapless mode E_1 exists and the corresponding k-independent wave function Ψ_1 is only distributed at the first and third channels with the same chirality. We can also find that the amplitude of the gapless ZLM in the two channels can be tuned by the ratio of coupling of adjacent ZLMs.

[1] Y. Ren, Z. Qiao, and Q. Niu, Rep. Prog. Phys. **79**, 066501 (2016).
[2] K. He, Y. Wang, and Q. K. Xue, Annu. Rev. Condens. Matter Phys. **9**, 329 (2018).
[3] J. Maciejko, T. L. Hughes, and S. C. Zhang, Annu. Rev. Condens. Matter Phys. **2**, 31 (2011).
[4] D. Xiao, W. Yao, and Q. Niu, Phys. Rev. Lett. **99**, 236809 (2007).
[5] Z. Wang, S. G. Cheng, X. Liu, and H. Jiang, Nanotechnology **32**, 402001 (2021).
[6] I. Martin, Y. M. Blanter, and A. F. Morpurgo, Phys. Rev. Lett. **100**, 036804 (2008).
[7] G. W. Semenoff, V. Semenoff, and F. Zhou, Phys. Rev. Lett. **101**, 087204 (2008).
[8] W. Yao, S. A. Yang, and Q. Niu, Phys. Rev. Lett. **102**, 096801 (2009).
[9] Z. Qiao, J. Jung, Q. Niu, and A. H. MacDonald, Nano Lett. **11**, 3453 (2011).
[10] K. Wang, T. Hou, Y. Ren, and Z. Qiao, Front. Phys. **14**, 23501 (2019).
[11] J. Jung, F. Zhang, Z. Qiao, and A. H. MacDonald, Phys. Rev. B **84**, 075418 (2011).
[12] A. Vaezi, Y. Liang, D. H. Ngai, L. Yang, and E.-A. Kim, Phys. Rev. X **3**, 021018 (2013).
[13] Y. Kim, K. Choi, J. Ihm, and H. Jin, Phys. Rev. B **89**, 085429 (2014).
[14] X. Bi, J. Jung, and Z. H. Qiao, Phys. Rev. B **92**, 235421 (2015).
[15] H. Pan, X. Li, F. Zhang, and S. A. Yang, Phys. Rev. B **92**, 041404(R) (2015).
[16] C. H. Lee, G. Kim, J. Jung, and H. Min, Phys. Rev. B **94**, 125438 (2016).
[17] L. Ju, Z. Shi, N. Nair, Y. Lv, C. Jin, J. Velasco, Jr., H. A. Bechtel, M. C. Martin, A. Zettl, J. Analytis, and F. Wang, Nature (London) **520**, 650 (2015).
[18] L.-J. Yin, H. Jiang, J.-B. Qiao, and L. He, Nat. Commun. **7**, 11760 (2016).
[19] J. Li, K. Wang, K. J. McFaul, Z. Zern, Y. Ren, K. Watanabe, T. Taniguchi, Z. H. Qiao, and J. Zhu, Nat. Nanotechnol. **11**, 1060 (2016).
[20] M. Kim, J. H. Choi, S. H. Lee, K. Watanabe, T. Taniguchi, S. H. Jhi, and H. J. Lee, Nat. Phys. **12**, 1022 (2016).
[21] H. Chen, P. Zhou, J. Liu, J. Qiao, B. Oezyilmaz, and J. Martin, Nat. Commun. **11**, 1202 (2020).
[22] Z. Qiao, J. Jung, C. Lin, Y. Ren, A. H. MacDonald, and Q. Niu, Phys. Rev. Lett. **112**, 206601 (2014).
[23] K. Wang, Y. Ren, X. Deng, S. A. Yang, J. Jung, and Z. Qiao, Phys. Rev. B **95**, 245420 (2017).
[24] J. Li, R.-X. Zhang, Z. Yin, J. Zhang, K. Watanabe, T. Taniguchi, C. Liu, and J. Zhu, Science **362**, 1149 (2018).
[25] J. R. Anglin and A. Schulz, Phys. Rev. B **95**, 045430 (2017).
[26] T. Hou, G. Cheng, W.-K. Tse, C. Zeng, and Z. Qiao, Phys. Rev. B **98**, 245417 (2018).
[27] S.-G. Cheng, H. Liu, H. Jiang, Q.-F. Sun, and X. C. Xie, Phys. Rev. Lett. **121**, 156801 (2018).
[28] B. Rzeszotarski, A. Mreńca-Kolasińska, and B. Szafran, Phys. Rev. B **101**, 115308 (2020).
[29] Y. Yang, Z. Jia, Y. Wu, R.-C. Xiao, Z. H. Hang, H. Jiang, and X. C. Xie, Sci. Bull. **65**, 531 (2020).
[30] C. Hu, V. Michaud-Rioux, W. Yao, and H. Guo, Phys. Rev. Lett. **121**, 186403 (2018).
[31] C. Hu, V. Michaud-Rioux, W. Yao, and H. Guo, Nano Lett. **19**, 4146 (2019).
[32] R. Xiang, T. Inoue, Y. Zheng, A. Kumamoto, Y. Qian, Y. Sato, M. Liu, D. Tang, D. Gokhale, J. Guo, K. Hisama, S. Yotsumoto, T. Ogamoto, H. Arai, Y. Kobayashi, H. Zhang, B. Hou, A. Anisimov, M. Maruyama, Y. Miyata *et al.*, Science **367**, 537 (2020).
[33] W. Jaskolski, M. Pelc, G. W. Bryant, L. Chico, and A. Ayuela, 2D Mater. **5**, 025006 (2018).
[34] P. Schweizer, C. Dolle, and E. Spiecker, Sci. Adv. **4**, eaat4712 (2018).
[35] K. Laubscher, D. Loss, and J. Klinovaja, Phys. Rev. Research **2**, 013330 (2020).
[36] X. Zhang, J. Hone, T. Taniguchi, K. Watanabe, Y. Wang, S. Yang, C. Zhang, M. Zhao, and S. Wang, Natl. Sci. Rev. **7**, 248 (2020).
[37] W. Kang, H. L. Stormer, L. N. Pfeiffer, K. W. Baldwin, and K. W. West, Nature (London) **403**, 59 (2000).
[38] T. Tudorovskiy and M. I. Katsnelson, Phys. Rev. B **86**, 045419 (2012).
[39] J. Lu, C. Qiu, L. Ye, X. Fan, M. Ke, F. Zhang, and Z. Liu, Nat. Phys. **13**, 369 (2017).
[40] J.-W. Dong, X.-D. Chen, H. Y. Zhu, Y. Wang, and X. Zhang, Nat. Mater. **16**, 298 (2017).
[41] F. Gao, H. Xue, Z. Yang, K. Lai, Y. Yu, X. Lin, Y. Chong, G. Shvets, and B. L. Zhang, Nat. Phys. **14**, 140 (2018).
[42] J. Noh, S. Huang, K. P. Chen, and M. C. Rechtsman, Phys. Rev. Lett. **120**, 063902 (2018).
[43] M. Yan, J. Lu, F. Li, W. Deng, X. Huang, J. Ma, and Z. Liu, Nat. Mater. **17**, 993 (2018).
[44] C. H. Lewenkopf and E. R. Mucciolo, J. Comput. Electron. **12**, 203 (2013).
[45] *Electronic Transport in Mesoscopic Systems*, edited by S. Datta (Cambridge University Press, Cambridge, 1995).
[46] M. P. L. Sancho, J. M. L. Sancho, and J. Rubio, J. Phys. F: Met. Phys. **14**, 1205 (1984).
[47] M. Ezawa and N. Nagaosa, Phys. Rev. B **88**, 121401(R) (2013).